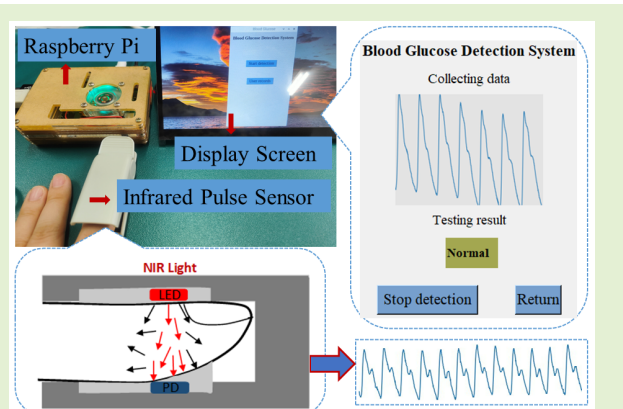


# Noninvasive Blood Glucose Detection System With Infrared Pulse Sensor and Hybrid Feature Neural Network

Yucen Yang<sup>ID</sup>, Jie Chen, Jie Wei<sup>ID</sup>, Zhikang Wang<sup>ID</sup>, Jiangning Song<sup>ID</sup>, Yuanting Zhang<sup>ID</sup>, Fellow, IEEE, Yuan Zhang<sup>ID</sup>, Senior Member, IEEE, and Jichao Zhao<sup>ID</sup>

**Abstract**—The rising prevalence of diabetes increases the demand for daily blood glucose (BG) detection, necessitating the urgent development of noninvasive BG detection systems. To enhance the convenience of BG monitoring, we employed infrared pulsed sensing (IPS) to capture photoplethysmography (PPG) signals. PPG signals effectively reflect changes in blood volume within the human body, providing rich information about BG. In this article, we designed a BG detection system based on an IPS and a deep hybrid feature neural network. By deploying IPS and deep learning algorithms on a Raspberry Pi, the system is equipped with data collection, analysis, prediction, and display capabilities for real-time BG monitoring. Previous studies relying on shallow machine learning for BG detection struggled to capture the complex underlying correlations between PPG signals and BG. Our proposed deep hybrid feature neural network model, DCC-Net, achieves end-to-end BG prediction by capturing different temporal and spatial features in PPG signals. The F2M fusion module combines multiscale and multilevel features, effectively modeling the intricate nonlinear relationship between PPG signals and BG, thereby improving classification performance. We recruited 290 participants and used IPS to collect PPG signals, constructing an IPS-PPG dataset. Testing DCC-Net on the IPS-PPG dataset yielded an impressive overall classification accuracy of 0.92, demonstrating its high accuracy. Furthermore, our model showed good generalization performance on the publicly available dataset PPG-BP. The proposed approach exhibits significant potential for advancing research and development in noninvasive BG detection systems.

**Index Terms**—Blood glucose (BG) classification, BG detection system, infrared pulse sensor, neural network, photoplethysmography (PPG).



Manuscript received 6 January 2024; accepted 26 February 2024. Date of publication 13 March 2024; date of current version 16 April 2024. This work was supported by the National Natural Science Foundation of China under Grant 62172340 and in part by the Natural Science Foundation of Chongqing under Grant cstc2021jcyj-msxmX0041 and Grant cstc2021jcyj-msxmX0968. The associate editor coordinating the review of this article and approving it for publication was Prof. Maryam Shojaei Baghini. (Yucen Yang and Jie Wei contributed equally to this work.) (Corresponding author: Yuan Zhang.)

This work involved human subjects or animals in its research. Approval of all ethical and experimental procedures and protocols was granted by the Ethnic Committee of The Ninth People's Hospital of Chongqing under Approval No. 2022-SCI-007.

Yucen Yang, Jie Wei, and Yuan Zhang are with the College of Electronic and Information Engineering, Southwest University, Chongqing 400715, China (e-mail: yuanzhang@swu.edu.cn).

Jie Chen is with the Department of Endocrinology, The Ninth People's Hospital of Chongqing, Beibei, Chongqing 400700, China.

Zhikang Wang and Jiangning Song are with the Biomedicine Discovery Institute and Department of Biochemistry and Molecular Biology, Monash University, Melbourne, VIC 3800, Australia.

Yuanting Zhang is with the Department of Electronic Engineering, Chinese University of Hong Kong, Hong Kong, SAR, China.

Jichao Zhao is with the Auckland Bioengineering Institute, University of Auckland, Auckland 1142, New Zealand.

Digital Object Identifier 10.1109/JSEN.2024.3373048

## I. INTRODUCTION

**D**IABETES is a chronic disease that affects people of all ages and is increasingly prevalent in younger populations [1]. It has also been a significant cause of death in patients hospitalized with Corona Virus Disease in 2019 [2]. Moreover, prolonged hyperglycemia (HA) damages various tissues, including the eyes and cardiovascular system, and triggers a series of complications that ultimately increase the mortality risk for patients. Data from the International Diabetes Federation (IDF) reveals that one in every ten individuals has diabetes on average [3]. Given the irreversible nature of diabetes, early detection and treatment are the most effective strategies. Therefore, preventing pre-HA becomes essential in managing the disease.

The rise of smart medicine and the increasing trend toward self-health awareness has generated a higher demand for affordable, small smart devices capable of measuring blood glucose (BG) levels [4]. BG research has evolved, transitioning from invasive to minimally invasive and finally to noninvasive methods. Noninvasive techniques for BG measurement

encompass infrared spectroscopy, Raman spectroscopy, optical coherence tomography, electrical resistance method, and body fluid testing, among others [5]. Photoplethysmography (PPG) is a noninvasive optical technique that detects microvascular changes in blood volume within tissues [6]. The fundamental principle of PPG, which is based on the varying sensitivity of different optical wavelengths to blood and other constituents, presents a PPG waveform that varies cyclically with the heartbeat [7]. BG detection based on PPG signals exhibits advantages over other noninvasive BG measurement technologies, such as portability, low cost, high safety, practicality, and versatility. A PPG signal can be obtained using a pulse sensor, typically comprising three main components: a light-emitting diode (LED), a photodiode (PD), and an analog front end (AFE). We have opted for a near-infrared LED as the light source, enabling us to capture the PPG signal with the highest glucose molecule content [4], [5]. By extracting relevant and specific features and constructing an algorithmic model to correlate these features with BG parameters, it becomes possible to predict BG levels. Due to the weak and low-frequency nature of the PPG signal, it is susceptible to interference. The majority of studies [8], [9], [10] preprocess PPG signals by denoising and removing baseline drift and focusing on manually selecting features using machine learning. However, manually selecting features may overlook some complex and specific characteristics. The chosen limited features are challenging to capture the intricate nonlinear relationship between PPG signals and BG. This not only affects the accuracy of BG detection but also increases the time cost of BG examination. Only a few researchers have attempted deep learning approaches, yet satisfactory results in BG classification have not been achieved. Deep learning not only captures surface features of the data but also progressively learns multilevel abstract features, thereby constructing more advanced and refined representations. Additionally, certain scholars have proposed solution concepts that still need to be explored for researching BG detection systems (BGDS).

This research builds upon the previous work conducted by our laboratory member Zhang et al. [8]. Zhang et al. [8] utilized a fitting-based sliding window algorithm for signal preprocessing and extracted 28 correlation features from the PPG signal. These features were subsequently employed in a support vector machine (SVM) and K-nearest neighbor (KNN) algorithm for BG classification prediction. Most scholars have adopted a similar approach in prior studies. Although this method laid the foundation for using PPG to predict BG levels, there is room for improvement in accuracy and computational complexity. Additionally, this approach has not undergone evaluation using publicly accessible datasets, nor has it been integrated into a platform for practical applications.

Therefore, we aim to develop a noninvasive BG detection method that is convenient, cost-effective, and highly accurate. The primary contributions of this article are as follows.

- 1) We have developed a noninvasive BGDS based on infrared pulsed sensing (IPS) and a deep hybrid feature neural network. The proposed high-accuracy DCC-Net was deployed into the Raspberry Pi 4B. This system enables real-time end-to-end BG detection using an

external IPS to capture the PPG signal, along with a small display to showcase the results.

- 2) To extract more specific features, we designed a 1-D convolutional neural network (CNN) encoder and a 1-D dilated causal convolutional encoder. These encoders incorporate a residual network to extract effective local feature vectors at different levels. The F2M fusion block combines the features from both encoders, merging the resulting global fine-grained features for classification, thereby enhancing the predictive performance of BG classification.
- 3) We recruited 290 subjects from a local hospital and collected high-quality fingertip PPG signals using IPS. The performance of the DCC-Net was evaluated on both the IPS-PPG dataset and the PPG-BP dataset, demonstrating superior performance on both sets.

## II. RELATED WORKS

For noninvasive glucose studies, early researchers demonstrated the feasibility of employing PPG signals to predict BG [11]. Monte-Moreno [12] studied the functional relationship between the shape of the PPG signal waveform and BG levels, revealing that elevated BG can lead to changes in human blood viscosity, vascular compliance, and other variations. Research employing PPG signals for BG prediction has primarily focused on three categories: acquiring high-quality PPG signals that accurately reflect variations in human physiological blood volume, extracting specific features associated with BG from PPG signals, and designing noninvasive BG detection smart health devices. We summarize the comparison of related work in Table I.

### A. Signal-Based Acquisition

Prabha et al. [9], Lee and Lee [13], and Prabha et al. [14] acquired PPG signals from the wrist area for BG prediction, while [15] used a mobile phone camera to capture eye images and extracted blood vessels as the region of interest (ROI), which were subsequently processed to predict BG. Meanwhile, BG prediction from fingertip PPG signals was performed by [8], [16], [17], and [18]. The amplitude and duration of the PPG signal are influenced by factors such as skin thickness and blood perfusion [19]. The PPG signal's inherent weak amplitude and low frequency make it susceptible to external influences. Experimental results have shown that compared to areas such as the wrist and earlobes, the fingertip can generate higher amplitude signals [20]. Consequently, the selection of sensors or other devices for PPG signal acquisition and the choice of the subject's body site hold critical importance.

### B. Specificity-Based Feature Selection

Zhang et al. [8] used a fitting-based sliding window algorithm to eliminate baseline drift, and extracted 28 features in both time and frequency domains using the Gaussian fitting method. These features were employed for classification, employing Gaussian SVM (GSVM), bagged trees (BTs), and KNN methods. Golap et al. [16] analyzed the PPG signal and its first- and second-order inverses, applying Fourier

**TABLE I**  
COMPARISON OF RELATED WORK

| Ref/Year    | Signal-based acquisition |                  | Specificity-based feature selection |   | BG detection-based application |   | Task                  |
|-------------|--------------------------|------------------|-------------------------------------|---|--------------------------------|---|-----------------------|
|             | Device                   | Measurement site | Model                               | Application                               |                                |   |                       |
| [8]/2020    | Smartphone Camera        | Finger           | GSVM/BT/KNN                         | -   | -                              | - | Triple classification |
| [9]/2022    | Empatica E4 wristband    | Wrist            | Extreme gradient boost regression   | -   | -                              | - | Prediction            |
| [10]/2021   | IPS                      | Finger           | Random Forest/XG Boost              | -   | -                              | - | Prediction            |
| [13]/2021   | IPS                      | Wrist            | CNN                                 | Wearable device based on wrist PPG signal | -                              | - | Prediction            |
| [14]/2021   | Wearable sensor          | Wrist            | SVM/XGBR                            | -   | -                              | - | Triple classification |
| [16]/2021   | Smartphone Camera        | Finger           | Multigene genetic programming       | -   | -                              | - | Prediction            |
| [18]/2023   | IPS                      | Finger           | Super vector machine                | -   | -                              | - | Binary classification |
| <b>Ours</b> | IPS                      | Finger           | DCC-Net                             | BGDS                                      | -                              | - | Triple classification |

analysis. They used a correlation-based genetic algorithm to identify the optimal 46 features, which were then utilized in a multigene genetic programming regression model for prediction. In another study [14], physiological information features of subjects, along with features selected using a hybrid approach involving mel-scale frequency cepstral coefficients, were used as inputs for an SVM and an extreme gradient boost (XGBR) in classification. The aforementioned methods are all aimed at preprocessing and extracting features from PPG signals, using less complex classifiers for BG prediction. However, they all involve intricate designs of feature extraction processes, and the task of selecting the most suitable features requires significant expertise and prior experience.

With the emergence of CNNs, which can automatically extract rich spatiotemporal features, they have been widely adopted in various fields such as computer vision and image recognition. In recent years, 1-D CNNs have been proposed for time series prediction as well [21]. Monte-Moreno [12] found that when predicting BG levels using linear regression, SVM, and neural network methods, even with a simple neural network, the model's performance demonstrated significant differences compared to linear regression and SVM methods. Haque et al. [17] extracted 46 features from PPG signals, their derivatives, and Fourier analysis, using a genetic algorithm for meticulous feature selection to address redundancy and overfitting concerns. They subsequently designed a deep neural network (DNN) to forecast BG levels. Taking inspiration from ResNets, Lee and Lee [13] employed a DNN to capture the nonlinear relationship between the PPG signal and its corresponding BG level. In a different approach, Armand-pour et al. [22] integrated attentional mechanisms and temporal features extracted by recurrent neural networks (RNNs) to capture the long-term dependencies in PPG signals for BG prediction. Deep learning methods demonstrate the potential for automated multiscale feature extraction, contributing to enhanced scalability. However, as network depth increases, challenges such as vanishing and exploding gradients may arise, and deep learning networks tend to involve a substantial number of parameters. Therefore, we have integrated a residual network mechanism into our model to alleviate gradient issues and developed a model to mitigate the problem of many parameters.

### C. BG Detection-Based Application

In previous studies, researchers used either smartphone or wristband sensors to obtain PPG signals with practical

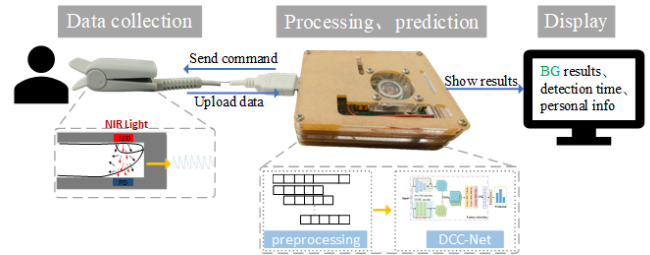


**Fig. 1.** General overview diagram of the BGDS that shows the functions of the system such as data collection, processing, prediction, and display.

applications in mind, but unfortunately did not realize the applications. Lee and Lee [13] developed a wearable device based on wrist PPG signals. It transmits data to a mobile device via Bluetooth, uploads it to the cloud for processing and analysis, and then returns the results to the mobile device. This process relies on stable data transmission, network connectivity, and expensive equipment, making it inconvenient and economically impractical for home BGDS.

In summary, our objective is to create an affordable and convenient BGDS. Our device is designed to conduct offline processing, eliminating the requirement for internet connectivity. This approach helps avoid data transmission delays and the associated costs of cloud services, all while ensuring user privacy.

## III. METHODS

We present a general overview diagram of our BGDS, including the system's hardware components and algorithmic integration, in Fig. 1, and the individual components are described in detail below.

### A. Principle and Structure of IPS

Compared to other areas of the human body, the fingertip PPG signal exhibits a higher signal amplitude and is less susceptible to factors such as skin color, age, gender, and skin thickness [19]. However, when capturing PPG signals, uncontrollable variables can still introduce various sources of high-frequency noise. Baseline drift might occur due to human respiration, body temperature, and micromovements originating from the sensor during measurement. Thus, the role of the sensor is crucial. Generally, the PPG signal in healthy individuals falls within the frequency range of 0.15–4 Hz [23], with some patients displaying tendencies to surpass this range.

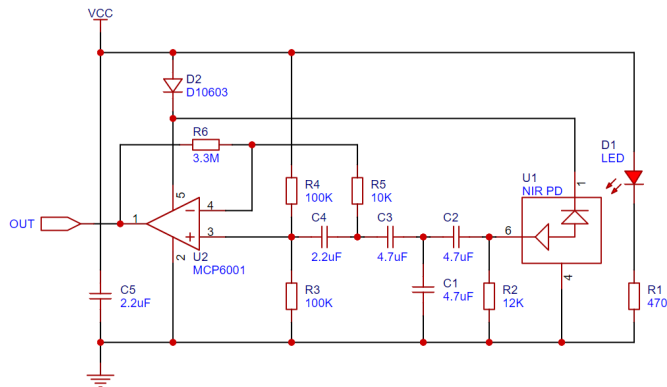


Fig. 2. Frontend circuit diagram of the IPS.

The frontend circuit diagram of the IPS is shown in Fig. 2. The IPS employs the PD with a frequency response in the near-infrared wavelength range, which can effectively capture the changes in the optical signal. The functional structure of the IPS is illustrated diagrammatically in Fig. 3. Using a near-infrared light source to irradiate the fingertips, the emitted light traverses the skin and experiences transmission, reflection, scattering, and absorption by some substances in the blood, where the absorbed light intensity consists of two components: the direct current (dc) component and the alternating current (ac) component. The ac component corresponds to the light intensity absorbed by arterial blood and reacts to variations in blood volume within the vessel. The light intensity that passes through the tissue is captured by a PD, which transforms the light intensity into an electrical signal, subsequently acquiring the PPG signal after digital-to-analog conversion. By the Lambert-Beer theorem [24], when a monochromatic beam of light with an intensity of  $I_0$  and a wavelength of  $\lambda$  is irradiated to the surface of the human body, the light intensity changes due to the absorption of light by the pulsatile blood. The resulting intensity of the transmitted light is denoted as  $I$

$$I = I_0(e^{-\varepsilon(\lambda)cd}). \quad (1)$$

$\varepsilon(\lambda)$  denotes the molar absorption coefficient for light of wavelength  $\lambda$ , which is a property of the substance itself,  $c$  denotes the concentration of the substance, and  $d$  denotes the optical length of light of wavelength  $\lambda$  that penetrates the substance. By varying (1), the relationship between the transmittance ratio  $T$  and the absorbance  $A$  is shown

$$T = \frac{I_0}{I} \quad (2)$$

$$A = -\ln T = \varepsilon(\lambda)cd. \quad (3)$$

It follows that when the incident light intensity  $I_0$ , the transmitted light intensity  $I$ , the molar absorption coefficient  $\varepsilon(\lambda)$ , and the optical range length of light penetrating the substance are known to be  $d$ , the concentration of the substance can be calculated as follows:

$$c = \frac{-\ln \left( \frac{I_0}{I} \right)}{\varepsilon(\lambda)cd}. \quad (4)$$

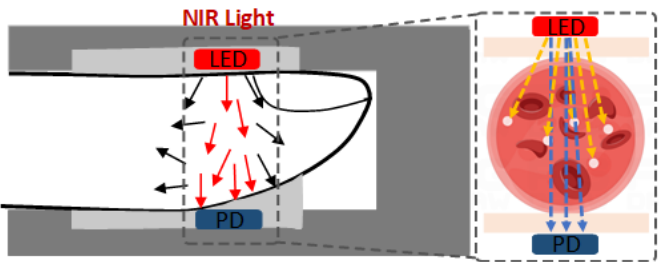


Fig. 3. Operating structure of the IPS schematic.

From (4), the concentration  $c$  of the substance to be measured is quantitatively related to the transmittance ratio  $T$  of the light, the molar extinction coefficient  $\varepsilon(\lambda)$ , and the optical range length  $d$  of the light penetrating the substance. When measuring BG concentration, the Lambert-Beer theorem applies to the photovoltaic volumetric pulse wave detection method described above. In this case, the change in absorbance of blood to light is the sum of the absorbance of glucose and other substances in the blood to that light beam

$$A = \varepsilon_0(\lambda)c_0d + \varepsilon(\lambda)cd \quad (5)$$

where  $\varepsilon_0(\lambda)$  denotes the molar extinction coefficient of glucose in the blood and  $c_0$  indicates the glucose concentration in the blood.  $\varepsilon(\lambda)$  and  $c$  denote the molar extinction coefficients and concentrations of other substances in the blood. The walls of the human blood vessels are found to change with the contraction and diastole of the heart, which leads to a change in the volume of blood in the vessels and, at the same time, makes the path length of the light change. According to (5), we can calculate the glucose concentration in the blood vessels. The Lambert-Beer theorem demonstrates a positive correlation between the concentration of a solution and its absorption of light intensity. It further notes that the magnitude of the irradiated light intensity does not impact the proportion of the solution absorbed. Variation in the waveform of the PPG signal changes in response to changes in the volume of blood in the vasculature, which includes changes in the signal mapped by glucose absorption of the light intensity.

### B. Data Acquisition

During our research, a thorough ethical review was conducted, and we carefully considered the security and lossless transmission of the data. The IPS HKG-07C+ was employed to capture the PPG signal at a sampling frequency of 200 Hz. Before data collection, the subjects were instructed to maintain an empty stomach in the morning and maintain a stationary seated position for 10 min. It was specified that the sensor should be affixed to the subject's left ring finger to record the PPG signal for 1 min. Simultaneously, healthcare professionals collected blood samples from the subjects and conducted glucose tests to acquire the corresponding glucose value levels. According to the standardized criteria set forth by the World Health Organization (WHO) and the IDF [25], we categorized the collected data into three categories: normal (NL), prehyperglycemic (PHA), and HA. Continuous glucose monitoring was conducted for participants with BG values

falling between the NL and HA categories, and the average value obtained served as the final BG label.

### C. BG Classification Algorithm Based on PPG Signal

**1) Data Preprocessing:** After filtering the data using a Butterworth filter, an imbalance was observed in the distribution of BG classification samples, with a relatively lower number of samples for the PHA and HA categories. This imbalance may lead to a decrease in the model's ability to identify these categories accurately. We employed a sliding window algorithm to segment the data and augment the sample size to mitigate the potential impact of data imbalance. Let the time series be  $S$ ,  $n$  denotes the length of the time series  $S$ , and  $X_i$  denotes sliced data, where  $i = \{0, 1, 2, \dots\}$ . The sliding window algorithm is formulated as follows:

$$X_i = S[i \cdot \text{step}:w + i \cdot \text{step}] \quad (6)$$

where  $w + i \cdot \text{step} \leq n$ , step denotes the sliding step, and  $w$  denotes the window size. In this article, we set step = 1 and  $w = 5$ .

**2) Differences Between Different Convolutions:** To capture fine-grained features at multiple scales in the signal, traditional convolution, causal convolution, and dilated convolution are used in DCC-Net for feature extraction, forming a hybrid feature neural network. The conventional convolution captures the sensory field by setting the size of the convolution kernel. Causal convolution [26] differs from the conventional convolution in that the value of its current moment  $t$  depends only on the values of the moment  $t - 1$  and the moments before it. This also makes the causal convolution complementary to zero in a way different from traditional convolution. In traditional 1-D signal processing, zeros are often filled symmetrically to the left and right of the sequence. In contrast, in causal convolution, zeros are filled only to the left of the dimension of the input tensor. The causal convolution is defined as follows: let the time series be  $X = \{x_1, x_2, \dots, x_t\}$  and to predict  $y_1, y_2, \dots, y_t$ , the filters  $F = \{f_1, f_2, \dots, f_k\}$ . Then the causal convolution at  $x_t$  is expressed as follows:

$$F * X = \left\{ \sum_{k=1}^K f_k x_{t-K} + k \right\}. \quad (7)$$

By incorporating the idea of holes into conventional convolutional operations, dilated convolution decreases network depth and increases receptive field [27]. The dilation rate controls the size of the holes, allowing customization of hole size to accommodate various time series lengths and task requirements. The dilated convolution operation can be defined as follows: given a time series  $X = \{x_1, x_2, \dots, x_t\}$ , filters  $F = \{f_1, f_2, \dots, f_k\}$ , and dilation factor rate, the dilated convolution at  $x_t$  is defined as follows:

$$F * X = \left\{ \sum_{k=1}^K f_k x_t - (K - k)\text{rate} \right\}. \quad (8)$$

The introduction of dilated convolution in causal convolution allows for an expanded perceptual field of the current neuron to the upper neuron, improving the prediction ability of causal convolution for longer remembered time series.

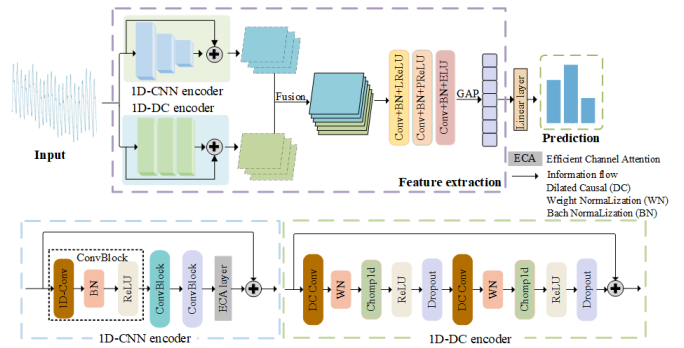


Fig. 4. Overall pipeline of the DCC-Net network.

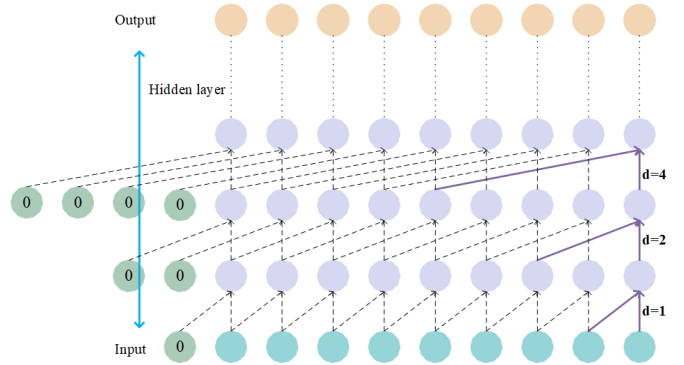


Fig. 5. Details of 1-D dc encoder.

The proposed neural network considers the data characteristics of the PPG signal. Utilizing a hybrid feature neural network model, it captures the PPG signal's rich temporal and spatial features, aiming to establish a mapping relationship between BG categories and PPG features.

**3) Network Architecture (DCC-Net):** As the PPG signal is a time series, extracting rich and consistent features that accurately reflect the data's characteristics and satisfy the requirements of wearable extension applications is crucial. To achieve this objective, we employed an improved ResCNN model to establish the framework. We introduced a 1-D dilated causal convolution to extract the temporal features, the proposed DCC-Net shown in Fig. 4. DCC-Net is a deep hybrid CNN-based model consisting of two encoders and a fusion block focusing on capturing multiscale temporal and spatial feature information for noninvasive glucose characterization. DCC-Net has a small number of participants and is easy to integrate into BG detection devices.

**a) Feature extraction:** We use both 1-D CNN encoder and 1-D dc encoder for feature extraction, and the details of the two encoders are shown in Figs. 4 and 5. The 1-D CNN encoder is structured with multiple convolutional blocks. We leverage 1-D convolutional blocks of varying scales to facilitate feature extraction. The employment of a multilayer network architecture with residual concatenation provides us with a heightened sensory field, thus enabling the effective acquisition of local information from PPG signals. Consequently, this setup aids in capturing multiscale feature vectors. On the other hand, the 1-D dc encoder consists of multilayer extended causal convolution and residual concatenation. Setting the dilation

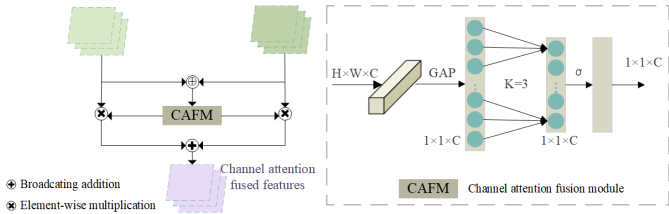


Fig. 6. F2M fusion block.

factor rate = {1, 2, 4} and stacking the multilayer hidden layers can obtain information about the sensory field and longer time series on the multilayer spatiotemporal scale, which can be used to extract rich fine-grained features. Moreover, the residual network plays an important role, and the residual connection merges multiple residual units to realize the fusion of different scale features. Furthermore, the residual network can also solve the degradation problem due to the increase in the number of network layers.

b) *F2M fusion block*: The detailed flow of the F2M fusion block is illustrated in Fig. 6. In the 1-D CNN encoder and 1-D dc encoder, the shallow network structure learns features such as contour and texture, while the deep structure learns abstract semantic features. However, as the features extracted by the two encoders have significant semantic inconsistencies, a simple sum of the features is inadequate for feature aggregation. Therefore, we employ the channel attention feature fusion module (CAFIM) to aggregate the features, with the structure shown in Fig. 6.

The CAFIM inherits the concept of the efficient channel attention (ECA) module [28]. It is based on the SE module. However, instead of using fully connected layers to learn channel attention information, CAFIM adopts  $1 \times 1$  convolution to reduce the number of parameters and prevent the reduction of channel dimensions and dependencies during the learning process. Despite having a small number of parameters, CAFIM offers significant performance improvements. First, CAFIM performs global average pooling (GAP) to compute the channel weights; the input feature map  $X \in \mathbb{R}^{H \times W \times C}$  is transformed into a feature vector of length  $C$ , where  $H$ ,  $W$ , and  $C$  represent the width, height, and channel dimensions, respectively. Subsequently, a 1-D convolution operation is applied using a convolution kernel size of 3. Finally, the weights  $W$  of each channel are obtained after applying the nonlinear activation function ReLU, as presented in the following equation:

$$W = R \left( \text{Conv} \left( \frac{1}{HW} \sum_{i=1}^H \sum_{j=1}^W x_{ij} \right) \right) \quad (9)$$

where Conv denotes 1-D convolution and  $R$  denotes the activation function ReLU. Feature fusion can be expressed as follows:

$$F = W \otimes X_1 + W \otimes X_2 \quad (10)$$

where  $F \in \mathbb{R}^{H \times W \times C}$  is a fused feature.  $W$  denotes the channel attention weight, which enables the network to be weighted

averaging between  $X_1$  and  $X_2$ .  $\otimes$  denotes the element-wise multiplication.

After fusing the feature vectors, global fine-grained features are further extracted. To improve the ReLU activation function from different angles, we replace it with LReLU, PReLU, and ELU activation functions. Using different activation functions in different layers allows for proper abstraction [21]. The output feature vector is then passed through a GAP operation to reduce the number of operations and parameters in the model. Finally, the linear classifier predicts the BG classification. The model loss is given as follows:

$$L = -\frac{1}{N} \sum_{i=1}^N \sum_{j=1}^C y_{ij} \log p_{ij} \quad (11)$$

where  $N$  represents the number of samples,  $C$  denotes the number of categories, with  $C = 3$  in this work,  $y$  represents the true labels of the samples, and  $p$  signifies the model's predicted probabilities for the samples. The algorithm flow of DCC-Net is shown in Algorithm 1.

#### Algorithm 1 DCC-Net Algorithm Flow

**Input:** S: Sequence of ppg signals after windowing, levels: blood glucose level  
**Output:** Result: NL, PHA or HA

- 1: Initialized the parameters of DCC-Net model
- 2: Extracting spatio-temporal features from 1D-CNN encoder as  $Y_1$
- 3: Extracting time series features from 1D-dc encoder as  $Y_2$
- 4: Fusing  $Y_1$  and  $Y_2$  features by F2M fusion block for  $Y = W \otimes Y_1 + W \otimes Y_2$
- 5:  $F_1 = \text{LReLU}(Bn(\text{Conv}(Y)))$   
 $F_2 = \text{PReLU}(Bn(\text{Conv}(F_1)))$   
 $Features = \text{ELU}(Bn(\text{Conv}(F_2)))$
- 6: **for**  $j \in \{1, 2, 3, \dots, K\}$  **do**
- 7:     Projected levels =  $\{(z_1, z_2, \dots, z_t)\} \leftarrow \text{DCC-Net}$   
 $levels = \{(x_1, x_2, \dots, x_t)\}$
- 8:      $Z_{i3} \leftarrow$  elements in Projected levels,  $X_{i3} \leftarrow$  predictive probability of the model for the sample.
- 9:     The loss function is defined as  
 $L = -\frac{1}{N} \sum_{i=1}^N \sum_{c=1}^3 Z_{i3} \log X_{i3}$
- 10:   Optimize the model parameters based on the loss function  $L$
- 11: **end for**
- 12:  $Results = \text{Linear}(\text{GAP}(Features))$
- 13: **return** Glucose classification result NL, PHA or HA

#### D. BGDS Design

1) *Hardware Connection*: We aim to design low-cost, high-precision noninvasive BGDS. We employed the Raspberry Pi 4B, featuring a 64-bit quad-core processor for development. The Raspberry Pi is directly connected to the IPS for data exchange through its built-in USB port. Meanwhile, a 7-in HDMI display with a resolution of  $1024 \times 600$  is employed for the system display, and the user experience is enhanced by designing an intuitive graphical user interface for data visualization. The hardware connections are depicted in Fig. 7.

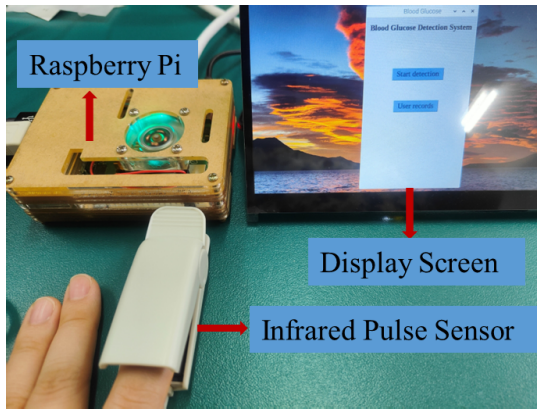


Fig. 7. System Hardware Connection.

**2) Algorithm Integration:** We tested different neural network parameters to achieve the highest accuracy during training and saved them as a model file. Subsequently, considering the ARM architecture of the CPU in Raspberry Pi 4B, deep learning frameworks and relevant libraries on the Raspberry Pi were configured to ensure effective deployment and execution of the model. Afterward, the pretrained DCC-Net model file was transferred to the Raspberry Pi. Real-time data was acquired through the Raspberry Pi USB interface, which was connected to the IPS. Then the obtained PPG data was fed into the DCC-Net for inference and testing, producing the corresponding prediction results. Finally, a graphical user interface (GUI) library was employed to develop the system interface, visualizing the process and outcomes of BG results.

#### IV. EXPERIMENTS AND RESULTS

##### A. Dataset

**1) IPS-PPG Dataset:** All records in the IPS-PPG dataset were collected from the Ninth People's Hospital of Chongqing under the ethical approval number 2022-SCI-007. The clinical dataset includes 153 female and 137 male participants, totaling 290, with ages ranging from 16 to 93 years. The participants have no other underlying diseases, as more detailed in Table II. The collected PPG signals are segmented into 5-s intervals. The data sample is further augmented using a sliding window algorithm, resulting in 6296 data instances. The specific categorized data are presented in Table III. Following data preprocessing, the dataset of 290 subjects is split based on subject identifiers with an 8:2 ratio, forming the training and testing sets which are mutually independent.

**2) PPG-BP Dataset:** The dataset originates from patients at the People's Hospital of Guilin, China, covering an age range of 20 to 89 years. It includes 219 participants, classified into two categories based on their BG levels: NL and diabetes, as shown in Table III. A more detailed description of the PPG-BP database can be found in [29].

##### B. Experimental Settings and Evaluation

The model was trained in a Python 3.8 environment using the PyTorch deep learning framework for algorithm evaluation. Through hyperparameter search, various combinations were explored, and the final experimental hyperparameter settings

**TABLE II**  
DEMOGRAPHICS OF THE LOCAL DATASET

| Metric  | Weight(kg) | Height(m) | Age(years) | BMI( $\text{kg}/\text{m}^2$ ) | BG( $\text{mmol}/\text{L}$ ) |
|---------|------------|-----------|------------|-------------------------------|------------------------------|
| Minimum | 42         | 1.42      | 16         | 16                            | 4                            |
| Maximum | 130        | 1.82      | 93         | 37.8                          | 11.2                         |
| Mean    | 60         | 1.62      | 45.7       | 24.4                          | 5.7                          |
| SD      | 12         | 0.08      | 15.4       | 4                             | 1.8                          |

**TABLE III**  
BG CATEGORIZATION

| Category | Clinical Dataset                    |                | PPG-BP Dataset |                |               |
|----------|-------------------------------------|----------------|----------------|----------------|---------------|
|          | BG Ranges( $\text{mmol}/\text{L}$ ) | Subjects(size) | Samples(size)  | Subjects(size) | Samples(size) |
| NL       | 3.9-6.0                             | 226            | 2712           | 181            | 512           |
| PHA      | 6.1-6.9                             | 24             | 1344           | 38             | 206           |
| HA       | 7.0-11.2                            | 40             | 2240           |                |               |

**TABLE IV**  
DCC-NET RESULTS

| BG Category      | Accuracy | Precision | Sensitivity | F1-score |
|------------------|----------|-----------|-------------|----------|
| Normal           | 0.92     | 0.90      | 0.85        | 0.90     |
| Prehyperglycemia | 0.95     | 0.94      | 0.94        | 0.90     |
| Hyperglycemia    | 0.97     | 0.96      | 0.99        | 0.96     |

are as follows: a batch size of 64, a learning rate of 0.00005 with Adam optimizer adjusting the learning rate automatically, and a total of 200 training iterations. After each training epoch, we evaluated the test set and saved the results. Hyperparameter optimization, training, and testing experiments of DCC-Net were implemented on a computer with a GPU of NVIDIA GeForce 3060. We selected the neural network parameters with the highest accuracy during training to be saved as the final network model for testing. The trained model will be deployed on the Raspberry Pi for testing. In our experiments, we evaluate the performance of the models based on various metrics, such as accuracy, precision, sensitivity, specificity, and F1-score.

##### C. Results

**1) Scoring Performance of DCC-Net:** Table IV displays the detailed results of BG classification by DCC-Net on the clinical dataset, with a weighted average accuracy, recall, sensitivity, and F1-score of 0.92, 0.91, 0.91, and 0.92, respectively, for BG classification. Among the three classifications of BG, the HA period performed the best with an accuracy of 0.97, a recall of 0.96, a sensitivity of 0.99, and an F1-score of 0.96. Other indicators for the three categories are also presented in detail. From Table IV, it is evident that DCC-Net has achieved superior results. Our model is able to identify subjects in the PHA and HA periods more accurately and with high sensitivity, which proves that the characteristics of subjects in the two periods are distinctly different and the model has the ability to distinguish between NL and abnormal people. However, due to the close proximity of blood glucose values in NL and PHA subjects, it is considered that they have similar characteristics. Additionally, the relatively smaller sample size of PHA subjects resulted in lower accuracy rates for the NL category.

We employed the T-SNE algorithm [30] to visualize the features extracted by DCC-Net. The T-SNE algorithm can reduce high-dimensional data to lower dimensions while preserving the global structure of the data. The observed feature distributions in Fig. 8 exhibit the following trends: 1) depicts

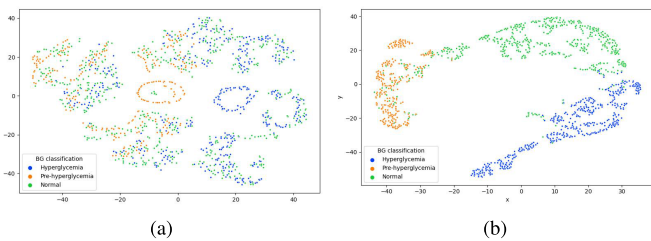


**Fig. 8.** T-SNE visualization of the BG classification feature representation on the IPS-PPG dataset, where (a) shows the feature visualization of the initial test set and (b) illustrates the output feature visualization of the test set after neural network training.

**TABLE V**  
PERFORMANCE COMPARISON WITH CLASSICAL METHODS

| Model          | Accuracy | Precision | Sensitivity | F1-score | Params(MB) |
|----------------|----------|-----------|-------------|----------|------------|
| LSTM [31]      | 0.73     | 0.75      | 0.75        | 0.70     | 6.92       |
| GRU [32]       | 0.68     | 0.68      | 0.67        | 0.68     | 0.88       |
| ResNet18 [33]  | 0.88     | 0.89      | 0.91        | 0.89     | 14.69      |
| <b>DCC-Net</b> | 0.92     | 0.93      | 0.91        | 0.92     | 1.03       |

**TABLE VI**  
PERFORMANCE COMPARISON WITH STATE-OF-THE-ART METHODS

| Model                     | Accuracy | Precision | Sensitivity | F1-score |
|---------------------------|----------|-----------|-------------|----------|
| Nirala <i>et al.</i> [34] | 0.75     | 0.76      | 0.74        | 0.75     |
| Zhang <i>et al.</i> [8]   | 0.81     | 0.81      | 0.80        | 0.80     |
| Prabha <i>et al.</i> [14] | 0.88     | 0.90      | 0.88        | 0.88     |
| <b>DCC-Net</b>            | 0.92     | 0.93      | 0.91        | 0.92     |

the feature distribution of the initial test set, showing that all features are mixed together without a discernible pattern and 2) illustrates the feature distribution after the output of DCC-Net, where data points from different categories tend to cluster together, with notable distinctions among the NL, PHA, and HA categories. This result indicates that DCC-Net demonstrates effectiveness in feature learning, enabling the effective differentiation of samples with varying BG levels.

**2) Comparison With Other Methods:** Experiments using long short-term memory (LSTM) [31] and gated recurrent unit (GRU) [32], which are more optimized than RNN, have revealed that both models extract a single feature and fail to achieve the desired high accuracy and lightweight requirements. ResNet [33], which applies the ideas of residual networks in DNN, has been shown to achieve higher accuracy than RNN-based models and exhibits good sensitivity to BG features. Therefore, our model combines the concepts of time series neural networks and residual networks, based on the results of the experiments with the aforementioned models, as shown in Table V. We implemented state-of-the-art methods [8], [14], [34] on the IPS-PPG dataset, and the results shown in Table VI indicate that our approach, DCC-Net, outperforms the existing methods in terms of accuracy, recall, sensitivity, and F1 score.

**3) Analysis of Ablation Experiment:** To demonstrate the effectiveness of our proposed module, we performed an ablation analysis on a clinical dataset, as shown in Table VII. We first trained the 1-D CNN (Baseline) model, which primarily extracts spatiotemporal features from PPG signals. Next, we trained a model composed of dilated causal convolutions combined with a residual network (dc). The dc model introduces dilated causal convolutions to capture longer range

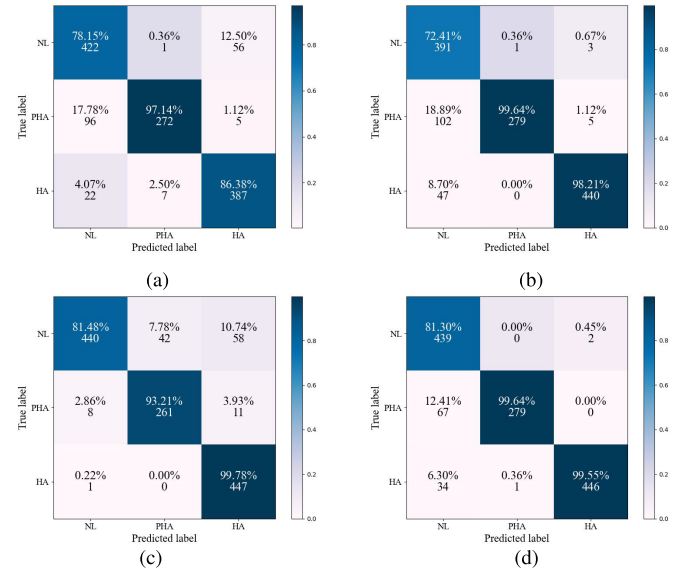


**Fig. 9.** Confusion matrix of ablation analysis on clinic datasets. (a) Baseline. (b) DC. (c) Baseline + dc. (d) DCC-Net.

**TABLE VII**  
ABLATION ANALYSIS OF DIFFERENT STRUCTURES

| Model           | Accuracy | Sensitivity | F1-score | Params(MB) |
|-----------------|----------|-------------|----------|------------|
| Baseline        | 0.85     | 0.85        | 0.85     | 0.98       |
| DC              | 0.88     | 0.87        | 0.87     | 0.23       |
| Baseline+DC     | 0.90     | 0.90        | 0.90     | 1.03       |
| Baseline+DC+CAF | 0.92     | 0.91        | 0.92     | 1.03       |

temporal dependencies. Subsequently, we trained a model that combines Baseline and dc, denoted as (Baseline + dc). The (Baseline + dc) model leverages the strengths of both Baseline and dc, enabling it to extract more comprehensive features. Additionally, to demonstrate the feature aggregation capability of the CAFM, we trained the final DCC-Net model with the inclusion of the CAFM. The results demonstrate that DCC-Net achieved the best results in all metrics, as shown in Table VII.

The confusion matrix for the four modules is shown in Fig. 9, which includes the number of samples predicted by the model and the corresponding percentages. The color shading of the squares corresponds to the number of samples, with darker colors indicating a higher number of samples predicted by the reclassification. The Baseline was more effective in classifying the PHA period and dc was significant in classifying the PHA and HA phases. The combination of the two (Baseline + dc) showed a significant improvement in the classification of the NL period of BG. By introducing CAFM, we enhanced the extracted features and improved the prediction results even further. Fig. 10 illustrates the receiver operating characteristic curve (ROC) for the ablation analysis. The five different color of curves in the figure represent the area under the curve (AUC) values of the ROC for the three blood glucose categories (NL, PHA, and HA), the macroaverage, and the microaverage, respectively. A curve closer to the upper-left corner with a larger AUC value indicates better classification performance of the model. DCC-Net achieves the highest AUC values, with an AUC of 1 for the HA category and 0.99 for both the PHA and the NL categories. This outcome signifies that DCC-Net excels in distinguishing between diabetic patients and NL individuals.

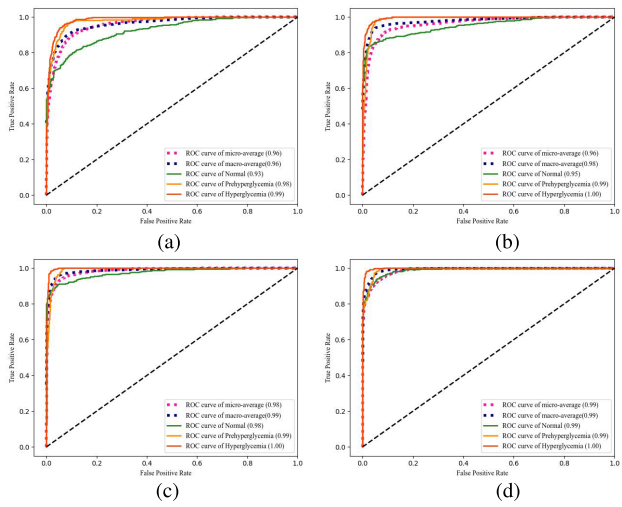


**Fig. 10.** ROC curves of ablation analyses on the IPS-PPG dataset, the closer the ROC curve is to the upper-left corner, the larger the AUC, indicating higher accuracy of the experiment. **(a)** Baseline. **(b)** DC. **(c)** Baseline + dc. **(d)** DCC-Net.

**TABLE VIII**  
ABLATION ANALYSIS OF THE PERFORMANCE OF THE DIFFERENT DILATION FACTORS

| Dilation factor | Pre-class F1-scores |      |      | Overall performance |      |
|-----------------|---------------------|------|------|---------------------|------|
|                 | NL                  | PHA  | HA   | Accuracy            | MF1  |
| 1,2,3           | 0.89                | 0.87 | 0.90 | 0.88                | 0.89 |
| <b>1,2,4</b>    | 0.90                | 0.90 | 0.96 | 0.92                | 0.92 |
| 1,2,5           | 0.88                | 0.86 | 0.95 | 0.90                | 0.89 |
| 1,2,8           | 0.87                | 0.88 | 0.95 | 0.90                | 0.90 |
| 1,3,9           | 0.93                | 0.83 | 0.92 | 0.90                | 0.89 |

Furthermore, to explore and identify the optimal combination of dilation factors, we conducted a series of experiments to assess the effectiveness of various dilation factor configurations on the performance of DCC-Net. Among the different combinations of dilation factors, the combination of dilation factors 1, 2, and 4 showed better performance in several evaluation metrics. Consequently, we ultimately selected it as the definitive dilation factor for DCC-Net, as shown in Table VIII. To summarize, DCC-Net shows the best performance in the ablation experiments. It can be concluded that the modules in the proposed DCC-Net network are effective.

**4) DCC-Net Experiments on the Public Dataset PPG-BP:** To demonstrate the generalization performance of our model, we conducted experiments on the publicly available PPG-BP dataset. Susana et al. [18] conducted binary classification on the PPG-BP dataset, and we also performed binary classification on the same dataset, with results presented in Table IX. DCC-Net achieved an average accuracy of 0.92, slightly surpassing the average of 0.91 reported by [18]. Furthermore, our model exhibits significant classification advantages in the NL category. Therefore, our model demonstrates good generalization capabilities.

#### D. Application

We deployed the trained algorithmic model into the Raspberry Pi to achieve real-time data processing and presentation. The IPS acquires fingertip data, which the Raspberry Pi

**TABLE IX**  
EXPERIMENTAL RESULTS OF DCC-NET ON PPG-BP

| Method             | Category | Accuracy | Recall | F1-Score |
|--------------------|----------|----------|--------|----------|
| Susana et al. [18] | NL       | 0.91     | 0.85   | 1.00     |
|                    | HA       | 0.91     | 1.00   | 0.90     |
| <b>DCC-Net</b>     | NL       | 0.95     | 0.87   | 0.91     |
|                    | HA       | 0.88     | 0.96   | 0.92     |

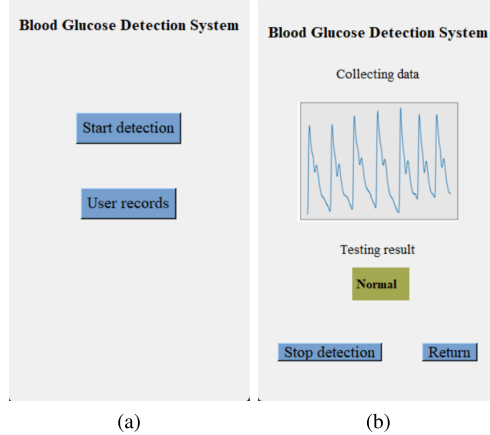


**Fig. 11.** **(a)** Initial display screen of the low-power platform. **(b)** BG detection page.

processes and feeds into a pretrained algorithmic model for real-time analysis. The detection outcomes are then showcased on a connected display, facilitating easy user access to the results. Our display is illustrated in Fig. 11. At the same time, the Raspberry Pi serves as a small-scale platform for testing and optimizing algorithmic models, accelerating the process of experimental innovation and development. We can achieve real-time data processing and presentation, which brings forth greater possibilities for the Internet of Things and embedded applications.

## V. CONCLUSION

We present a deep hybrid feature neural network model based on IPS and design a method for real-time BG detection without requiring networking, thereby forming a practical BGDS. The hardware components of the BGDS include a Raspberry Pi, an IPS, and a display. The deep learning algorithm is integrated into the Raspberry Pi, enabling real-time data acquisition, analysis, prediction, and display. Among various parts of the human body, the fingers are considered the optimal location for IPS to acquire PPG signals. Our proposed DCC-Net captures the glycemic characteristics of raw PPG signals acquired using IPS. We utilize multiscale convolution to extract diverse BG features, eliminating the need for intricate signal preprocessing and manual feature extraction. The model achieves high classification accuracy with minimal parameters, resulting in shortened training time and enhanced system efficiency. In our experiments, BG classification using DCC-Net on the IPS-PPG dataset yielded an overall classification accuracy of 0.92. Furthermore, a generalizable validation was conducted on the PPG-BP dataset, resulting in advanced results that demonstrate the effectiveness of our approach. The BGDS not only addresses the need

for universal family BG health monitoring but also holds significant implications for the research on BG classification.

In future work, we plan to expand the dataset further to enhance the system's performance. Additionally, we aim to upgrade the proposed strategy for quantitative measurement of BG levels, thereby improving the system's applicability and making it more suitable for a wide range of application scenarios.

## REFERENCES

- [1] D. J. Magliano, J. W. Sacre, J. L. Harding, E. W. Gregg, P. Z. Zimmet, and J. E. Shaw, "Young-onset type 2 diabetes mellitus—Implications for morbidity and mortality," *Nature Rev. Endocrinol.*, vol. 16, no. 6, pp. 321–331, Jun. 2020.
- [2] G. Corona et al., "Diabetes is most important cause for mortality in COVID-19 hospitalized patients: Systematic review and meta-analysis," *Rev. Endocrine Metabolic Disorders*, vol. 22, no. 2, pp. 275–296, Jun. 2021.
- [3] International Diabetes Federation, 10th ed. Brussels, Belgium: IDF Diabetes Atlas, 2021. [Online]. Available: <https://www.diabetesatlas.org>
- [4] A. M. Joshi, P. Jain, S. P. Mohanty, and N. Agrawal, "IGLU 2.0: A new wearable for accurate non-invasive continuous serum glucose measurement in IoMT framework," *IEEE Trans. Consum. Electron.*, vol. 66, no. 4, pp. 327–335, Nov. 2020.
- [5] B. Alsunaidi, M. Althobaiti, M. Tamal, W. Albaker, and I. Al-Naib, "A review of non-invasive optical systems for continuous blood glucose monitoring," *Sensors*, vol. 21, no. 20, p. 6820, Oct. 2021.
- [6] J. Allen, "Photoplethysmography and its application in clinical physiological measurement," *Physiolog. Meas.*, vol. 28, no. 3, pp. 1–39, Mar. 2007.
- [7] Y. Sun and N. Thakor, "Photoplethysmography revisited: From contact to noncontact, from point to imaging," *IEEE Trans. Biomed. Eng.*, vol. 63, no. 3, pp. 463–477, Mar. 2015.
- [8] G. Zhang et al., "A noninvasive blood glucose monitoring system based on smartphone PPG signal processing and machine learning," *IEEE Trans. Ind. Informat.*, vol. 16, no. 11, pp. 7209–7218, Nov. 2020.
- [9] A. Prabha, J. Yadav, A. Rani, and V. Singh, "Intelligent estimation of blood glucose level using wristband PPG signal and physiological parameters," *Biomed. Signal Process. Control*, vol. 78, Sep. 2022, Art. no. 103876.
- [10] S. Sen Gupta, T.-H. Kwon, S. Hossain, and K.-D. Kim, "Towards non-invasive blood glucose measurement using machine learning: An all-purpose PPG system design," *Biomed. Signal Process. Control*, vol. 68, Jul. 2021, Art. no. 102706.
- [11] A. Hina and W. Saadeh, "Noninvasive blood glucose monitoring systems using near-infrared technology—A review," *Sensors*, vol. 22, no. 13, p. 4855, Jun. 2022.
- [12] E. Monte-Moreno, "Non-invasive estimate of blood glucose and blood pressure from a photoplethysmograph by means of machine learning techniques," *Artif. Intell. Med.*, vol. 53, no. 2, pp. 127–138, 2011.
- [13] E. Lee and C. Lee, "PPG-based smart wearable device with energy-efficient computing for mobile health-care applications," *IEEE Sensors J.*, vol. 21, no. 12, pp. 13564–13573, Jun. 2021.
- [14] A. Prabha, J. Yadav, A. Rani, and V. Singh, "Design of intelligent diabetes mellitus detection system using hybrid feature selection based XGBoost classifier," *Comput. Biol. Med.*, vol. 136, Sep. 2021, Art. no. 104664.
- [15] S. Ghosal, A. Kumar, V. Udutoalapally, and D. Das, "GluCam: Smartphone based blood glucose monitoring and diabetic sensing," *IEEE Sensors J.*, vol. 21, no. 21, pp. 24869–24878, Nov. 2021.
- [16] M. A.-U. Golap, S. M. T. U. Raju, M. R. Haque, and M. M. A. Hashem, "Hemoglobin and glucose level estimation from PPG characteristics features of fingertip video using MGCP-based model," *Biomed. Signal Process. Control*, vol. 67, May 2021, Art. no. 102478.
- [17] M. R. Haque, S. M. T. U. Raju, M. A. Golap, and M. M. A. Hashem, "A novel technique for non-invasive measurement of human blood component levels from fingertip video using DNN based models," *IEEE Access*, vol. 9, pp. 19025–19042, 2021.
- [18] E. Susana, K. Ramli, P. D. Purnamasari, and N. H. Apriantoro, "Non-invasive classification of blood glucose level based on photoplethysmography using time-frequency analysis," *Information*, vol. 14, no. 3, p. 145, Feb. 2023.
- [19] J. Fine et al., "Sources of inaccuracy in photoplethysmography for continuous cardiovascular monitoring," *Biosensors*, vol. 11, no. 4, p. 126, 2021.
- [20] R. Lundström, H. Dahlqvist, M. Hagberg, and T. Nilsson, "Vibrotactile and thermal perception and its relation to finger skin thickness," *Clin. Neurophysiol. Pract.*, vol. 3, pp. 33–39, Sep. 2018.
- [21] X. Zou, Z. Wang, Q. Li, and W. Sheng, "Integration of residual network and convolutional neural network along with various activation functions and global pooling for time series classification," *Neurocomputing*, vol. 367, pp. 39–45, Nov. 2019.
- [22] M. Armandpour, B. Kidd, Y. Du, and J. Z. Huang, "Deep personalized glucose level forecasting using attention-based recurrent neural networks," in *Proc. Int. Joint Conf. Neural Netw. (IJCNN)*, Jul. 2021, pp. 1–8.
- [23] J. Moraes, M. Rocha, G. Vasconcelos, J. V. Filho, V. de Albuquerque, and A. Alexandria, "Advances in photoplethysmography signal analysis for biomedical applications," *Sensors*, vol. 18, no. 6, p. 1894, Jun. 2018.
- [24] I. Oshina and J. Spigulis, "Beer-Lambert law for optical tissue diagnostics: Current state of the art and the main limitations," *J. Biomed. Opt.*, vol. 26, no. 10, Oct. 2021, Art. no. 100901.
- [25] "Definition and diagnosis of diabetes mellitus and intermediate hyperglycaemia: Report of a WHO/IDF consultation," World Health Organization, Geneva, Switzerland, pp. 1–50.
- [26] T. J. Brazil, "Causal-convolution—A new method for the transient analysis of linear systems at microwave frequencies," *IEEE Trans. Microw. Theory Techn.*, vol. 43, no. 2, pp. 315–323, Feb. 1995.
- [27] H. Ma, C. Chen, Q. Zhu, H. Yuan, L. Chen, and M. Shu, "An ECG signal classification method based on dilated causal convolution," *Comput. Math. Methods Med.*, vol. 2021, pp. 1–10, Feb. 2021.
- [28] Q. Wang, B. Wu, P. Zhu, P. Li, W. Zuo, and Q. Hu, "ECA-Net: Efficient channel attention for deep convolutional neural networks," in *Proc. IEEE/CVF Conf. Comput. Vis. Pattern Recognit. (CVPR)*, Jun. 2020, pp. 11534–11542.
- [29] Y. Liang, Z. Chen, G. Liu, and M. Elgendi, "A new, short-recorded photoplethysmogram dataset for blood pressure monitoring in China," *Sci. Data*, vol. 5, no. 1, pp. 1–7, Feb. 2018.
- [30] L. van der Maaten and G. Hinton, "Visualizing data using t-SNE," *J. Mach. Learn. Res.*, vol. 9, no. 11, pp. 2579–2605, 2008.
- [31] S. Hochreiter and J. Schmidhuber, "Long short-term memory," *Neural Comput.*, vol. 9, no. 8, pp. 1735–1780, Nov. 1997.
- [32] R. Fu, Z. Zhang, and L. Li, "Using LSTM and GRU neural network methods for traffic flow prediction," in *Proc. 31st Youth Acad. Annu. Conf. Chin. Assoc. Autom. (YAC)*, Nov. 2016, pp. 324–328.
- [33] K. He, X. Zhang, S. Ren, and J. Sun, "Deep residual learning for image recognition," in *Proc. IEEE Conf. Comput. Vis. Pattern Recognit. (CVPR)*, Jun. 2016, pp. 770–778.
- [34] N. Nirala, R. Periyasamy, B. K. Singh, and A. Kumar, "Detection of type-2 diabetes using characteristics of toe photoplethysmogram by applying support vector machine," *Biocybern. Biomed. Eng.*, vol. 39, no. 1, pp. 38–51, Jan. 2019.